

Article

Exploring Different Binders for a LiFePO₄ Battery, Battery Testing, Modeling and Simulations

Joseph Paul Baboo^{1,2}, Mudasir A. Yattoo¹ , Matthew Dent¹, Elaheh Hojaji Najafabadi¹, Constantina Lekakou^{1,*} , Robert Slade², Steven J. Hinder¹  and John F. Watts¹

¹ Department of Mechanical Engineering Sciences, University of Surrey, Guildford GU2 7XH, UK; josefpaul@gmail.com (J.P.B.); muda.amu@gmail.com (M.A.Y.); m.j.dent@surrey.ac.uk (M.D.); e.hojajinajafabadi@surrey.ac.uk (E.H.N.); s.hinder@surrey.ac.uk (S.J.H.); j.watts@surrey.ac.uk (J.F.W.)
² Department of Chemistry, University of Surrey, Guildford GU2 7XH, UK; r.slade@surrey.ac.uk
* Correspondence: c.lekakou@surrey.ac.uk

Abstract: This paper focuses on the LiFePO₄ (LFP) battery, a classical and one of the safest Li-ion battery technologies. To facilitate and make the cathode manufacture more sustainable, two Kynar[®] binders (Arkema, France) are investigated which are soluble in solvents with lower boiling points than the usual solvent for the classical PVDF binder. Li-LFP and graphite-Li half cells and graphite-LFP full cells are fabricated and tested in electrochemical impedance spectroscopy, cyclic voltammetry (CV) and galvanostatic charge-discharge cycling. The diffusion coefficients are determined from the CV plots, employing the Rendles-Shevchik equation, for the LFP electrodes with the three investigated binders and the graphite anode, and used as input data in simulations based on the single-particle model. Microstructural and surface composition characterization is performed on the LFP cathodes, pre-cycling and after 25 cycles, revealing the aging effects of SEI formation, loss of active lithium, surface cracking and fragmentation. In simulations of battery cycling, the single particle model is compared with an equivalent circuit model, concluding that the latter is more accurate to predict “future” cycles and the lifetime of the LFP battery by easily adjusting some of the model parameters as a function of the number of cycles on the basis of historical data of cell cycling.

Keywords: LFP battery; degradation; binders; diffusion coefficients; single particle model; equivalent circuit model; simulations



Citation: Baboo, J.P.; Yattoo, M.A.; Dent, M.; Hojaji Najafabadi, E.; Lekakou, C.; Slade, R.; Hinder, S.J.; Watts, J.F. Exploring Different Binders for a LiFePO₄ Battery, Battery Testing, Modeling and Simulations. *Energies* **2022**, *15*, 2332. <https://doi.org/10.3390/en15072332>

Academic Editor: Seung-Joo Kim

Received: 20 February 2022

Accepted: 21 March 2022

Published: 23 March 2022

Publisher's Note: MDPI stays neutral with regard to jurisdictional claims in published maps and institutional affiliations.



Copyright: © 2022 by the authors. Licensee MDPI, Basel, Switzerland. This article is an open access article distributed under the terms and conditions of the Creative Commons Attribution (CC BY) license (<https://creativecommons.org/licenses/by/4.0/>).

1. Introduction

LiFePO₄ (LFP) batteries consist of a LiFePO₄-based cathode and graphite-based anode and are one of the safest types of Li-ion battery [1]. Safety is of particular concern for transport applications, namely electric vehicles and hybrid electric aircraft or space vehicles [2]. Given the low power density of LFP batteries, especially in charge, hybridization with supercapacitors [3–10] makes possible to raise the power while shifting the high rate burden to the supercapacitor [3]. The aging of the Li-ion batteries starts with the formation of the solid-electrolyte interface (SEI) at the electrodes-electrolyte interface, in fact from the first cycle, which controls the Li⁺ ion diffusion [11] while further pore clogging diminishes diffusion and ultimately leads to capacity reduction. Many cycles of Li⁺ ion intercalation and deintercalation strain the battery materials [12] and may cause cracking in the electrodes, which reduces conductivity while more SEI is formed in the newly formed crack surface, both reducing the amount of active material [11]. Heat generation is substantial especially at high operating currents and accelerates battery aging, sometimes also leading to thermal runaway [13,14]. Electrode thickness further controls the performance of Li-ion batteries, where while a thick electrode provides a large amount of active material, it also reduces overall Li⁺ ion diffusion which lowers battery rate performance and, consequently, power density [15]. LFP cathodes combined directly with a Li foil anode exhibit high performance

but are under the additional risk of dendritic growth on the Li anode, accelerated at high currents [16,17].

Materials processing and manufacturing of electrode coatings is highly dependent on the binder material which determines the solvent to be used in the process of slurry formation and coating. Polyvinylidene fluoride (PVDF) is the standard, high performance binder used for Li-ion batteries and supercapacitors including an organic or lithium-ion electrolyte [1,6]. However, the solvent employed, N-methyl-2-pyrrolidone (NMP), is highly toxic and has a high boiling point at 203 °C. Water-soluble or water-dispersed binders [18] such as gums [19], SBR (styrene-butadiene rubber) [4,20] or PEDOT:PSS [21] can be used in supercapacitors or the graphite anode in Li-ion batteries [22], where after coating they can be thoroughly dried under vacuum and heat so the electrodes contain no moisture when used in the electrochemical device. However, aqueous slurries are not advised for the LFP unless the LFP particles are protected with a coating shell [23]. Alternatively, Jeong et al. [24] used an ionic liquid solvent for natural cellulose used as a binder in LFP electrodes. In this study, we are investigating two PVDF-copolymer binders that are soluble in a wide range of organic solvents, some of them of a low boiling point. These binders have been used in the electrospinning [25–27] of mats on separators for Li-ion batteries, hence, they have proven compatible with Li-ion electrolytes.

Our study involves the fabrication and comprehensive characterization of half and full battery cells, including electrochemical testing of these cells, microstructural examination and surface analysis of their electrodes pre-cycling and postmortem after the cells have been cycled. Furthermore, battery simulation is performed to predict battery cycling. Two types of models have been traditionally used for batteries. Physicochemical process models and equivalent electric circuit models. Our group have developed comprehensive physicochemical models for supercapacitors [28–30] and lithium-sulfur batteries [30–34] that take into account the pore size distribution of the electrodes in the ion transport. However, unlike supercapacitors and lithium-sulfur batteries, ion transport in LFP batteries is dominated by the diffusion through the solid LFP particles in the cathode and graphite particles in the anode, with free and easy transport through the large interparticle space. If SEI formation and pore clogging reduces significantly this interparticle distance, this would affect the value of the diffusion coefficient. Hence, the Newman's single particle model (SPM) is a popular model for Li-ion batteries [35–38], where Li^+ ion diffusion is simulated through a phenomenological anode particle and a phenomenological cathode particle with the redox reactions taking place at the particle surface, at the electrode-electrolyte interface, following the Butler-Volmer equation expressing the overpotential. In recent papers, variation of the phenomenological particle diameter is allowed [38] to simulate graded electrodes, for example. Equivalent electric circuit models (EECM) with fits of the open circuit potential from experimental data [39,40] are popular for the energy and power management, offering the advantage of rapid runs and easy integration with control algorithms in the s-domain (after the Laplace transform from the time t-domain). Both SPM and EECM are employed and evaluated in this study. Furthermore, we are using the cyclic voltammetry of half cells at different scan rates to determine the diffusion coefficient of the Li^+ ions in the anode and cathode, and these values are inputted as property data in the SPM simulations.

2. LFP Battery Models

Two types of models are presented in this study. The first is the classical single particle (SP) model, considering the diffusion and electrochemical processes, and the second is an equivalent electric circuit (EEC) model at system level.

2.1. Single Particle Model

The single particle model represents each battery electrode as a single particle on the basis of two key assumptions: the current supplied to the battery is small and the electrolyte conductivity is large [41], so that the electrolyte concentration and current are constant

throughout the electrolyte. To determine the concentration of lithium ions in each particle as a function of time and particle radius, Fick's second law of diffusion is applied:

$$\frac{\partial C_{s,j}}{\partial t} = \frac{D_{s,j}}{r^2} \frac{\partial}{\partial r} \left(r^2 \frac{\partial C_{s,j}}{\partial r} \right) \quad (1)$$

where $C_{s,j}$ is the lithium-ion concentration in solid phase j (subscript j denotes the positive particle electrode p or the negative particle electrode n), t is time, r is the radial coordinate in the particle and $D_{s,j}$ is the lithium ion diffusion coefficient in solid phase j . The initial concentration condition $C_{s,int,j}$ in Equation (2) is equal to zero for the graphite anode and $0.02282 \text{ mol cm}^{-3}$ for the LFP cathode:

$$C_{s,j}|_{t=0} = C_{s,int,j} \quad (2)$$

Boundary conditions include symmetry at $r = 0$ of each particle electrode:

$$\left. \frac{\partial C_{s,j}}{\partial r} \right|_{r=0} = 0 \quad (3)$$

and a boundary condition for the lithium flux at the surface ($r = R_j$) of each particle, J_j :

$$\left. \frac{\partial C_{s,p}}{\partial r} \right|_{r=R_p} = \frac{J_p}{D_{s,p}} \quad (4)$$

$$\left. \frac{\partial C_{s,n}}{\partial r} \right|_{r=R_n} = -\frac{J_n}{D_{s,n}} \quad (5)$$

The molar flux of lithium ions at the surface of each electrode J_j is calculated by the relation:

$$J_j = \frac{I}{FA_j} \quad (6)$$

where I is the current applied to the cell, F is the Faraday's constant and A_j is the total electroactive surface area of the electrode, calculated by the following relation:

$$A_j = \frac{3\varepsilon_j V_j}{R_j} \quad (7)$$

where ε_j is the electrode particle volume fraction, R_j is the electrode particle radius and V_j is the total volume of that electrode. The state of charge x_j of the electrodes is given with respect to the maximum lithium concentration of the electrode, $C_{s,j,max}$:

$$x_{j,surf} = \frac{C_{s,j,surf}}{C_{s,j,max}} \quad (8)$$

The initial state of charge of the electrodes is given by the following equation:

$$x_{int,j} = \frac{C_{s,int,j}}{C_{s,j,max}} \quad (9)$$

where $C_{s,int,j}$ is the initial concentration of the electrode.

The Butler-Volmer equation is used to calculate the overpotential of the electrodes η_j :

$$J_j = k_j C_{s,j,max} c_e^{0.5} (1 - x_{j,surf})^{0.5} x_{j,surf}^{0.5} \left[\exp\left(\frac{0.5F}{RT} \eta_j\right) - \exp\left(-\frac{0.5F}{RT} \eta_j\right) \right] \quad (10)$$

where k_j is the temperature dependent reaction rate constant, R is the ideal gas constant and c_e is the electrolyte concentration in solution phase. The overpotential η_j is expressed as follows:

$$\eta_j = \phi_{1,j} - \phi_{2,j} - U_j \quad (11)$$

where $\phi_{1,j}$ is the solid phase potential, $\phi_{2,j}$ is the solution phase potential and U_j is the open circuit voltage of the electrode which is dependent on the state of charge of the electrode. In this study, empirical relations were used for the U_p of the LFP cathode and the U_n of the graphite anode taken from Schimpe et al. [42] which were fitted to open circuit voltage data from the paper of Safari et al. [43]. The solution phase is simplified as a nonlinear resistor so the potential drop between the positive and negative electrodes in the solution phase is given by the equation:

$$\phi_{2,p} - \phi_{2,n} = IR_{cell} \quad (12)$$

The cell voltage can be expressed as the difference of solid phase potential between the positive and negative electrodes:

$$V_{cell} = \phi_{1,p} - \phi_{1,n} \quad (13)$$

An explicit expression for the cell voltage can be derived from Equations (10)–(13):

$$V_{cell} = U_p - U_n + \frac{2RT}{F} \ln \left(\frac{\sqrt{m_p^2 + 4} + m_p}{2} \right) + \frac{2RT}{F} \ln \left(\frac{\sqrt{m_n^2 + 4} + m_n}{2} \right) + IR_{cell} \quad (14)$$

where:

$$m_p = \frac{I}{Fk_p S_p C_{s,p,max} c_e^{0.5} (1 - x_{p,surf})^{0.5} x_{p,surf}^{0.5}} \quad (15)$$

$$m_n = \frac{I}{Fk_n S_n C_{s,n,max} c_e^{0.5} (1 - x_{n,surf})^{0.5} x_{n,surf}^{0.5}} \quad (16)$$

Using Equation (14), the cell voltage can be calculated directly from the state of charge of the positive and negative electrodes. The high reaction constant values of $k_p = 1 \times 10^{-9} \text{ m}^{2.5}/\text{mol}^{0.5} \text{ s}$ and $k_n = 5 \times 10^{-11} \text{ m}^{2.5}/\text{mol}^{0.5} \text{ s}$ [44] were used for the LFP cathode and the graphite anode, respectively. An explicit finite volume/finite difference scheme [45,46] has been used for the solution of the diffusion partial differential Equation (1), adjusting the time step, Dt , so that: $D_{s,j} Dt / Dr^2 \leq 0.25$ to ensure numerical stability (Dr is the spatial interval in the radial direction r of the particle).

2.2. Equivalent Circuit Model

Figure 1 presents the general equivalent electric circuit model created to represent a cycled battery cell. It consists of constant phase elements (CPE) and resistances (R). A CPE is a hybrid capacitor-resistor with the real and imaginary impedance components, Zre_{CPE} and Zim_{CPE} , given by the relations:

$$Zre_{CPE} = \frac{1}{Q\omega^n} \cos\left(-\frac{n\pi}{2}\right) \quad Zim_{CPE} = \frac{1}{Q\omega^n} \sin\left(-\frac{n\pi}{2}\right) \quad (17)$$

where ω is the angular frequency and n and Q are empirical parameters: if $n = 1$, the CPE is a pure capacitor of capacitance Q ; if $n = 0$, the CPE is a pure resistor of resistance $1/Q$.

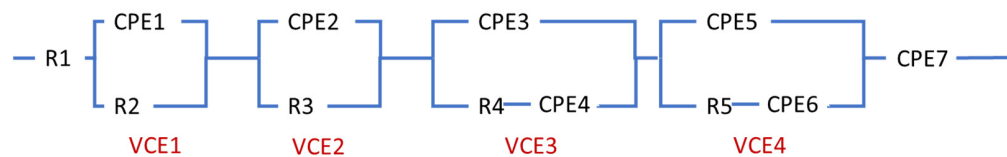


Figure 1. EECM of a cycled battery cell.

The EECM components represent the following battery characteristics: R1 represents the electrolyte and electrodes resistance, the Voigt circuit elements, VCE1 and VCE2 represent the contact resistance at the anode/current collector and cathode/current collector interfaces, VCE3 and VCE4 represent ion transfer through the pore hierarchy of the solid electrolyte interfaces (SEI) and electrode coating at the anode and the cathode. The parameters of the EECM will be fitted from the Nyquist curve of electrochemical impedance spectroscopy data in this study. The EECM will be then employed to simulate the galvanostatic charge-discharge stages of battery cycling, where the angular frequency, ω (in rad s^{-1}), is considered as a function of the charge or discharge time, t_{charge} and $t_{\text{discharge}}$, respectively [4,47]:

$$\omega = \frac{\pi}{t_{\text{charge}}} \text{ or } \omega = \frac{\pi}{t_{\text{discharge}}} \quad (18)$$

The total battery voltage is the sum of the EECM voltage and the open circuit voltage, V_{OC} , according to the relation:

$$V_{TOT} = V_{R1} + V_{VCE1} + V_{VCE2} + V_{VCE3} + V_{VCE4} + V_{CPE7} + V_{OC} \quad (19)$$

The voltage differences in Equation (19) are calculated as: V_{R1} is the product of R1 and the current; V_{VCE1} , V_{VCE2} , V_{VCE3} , V_{VCE4} , V_{VCE7} are calculated as V_{CPE1} , V_{CPE2} , V_{CPE3} , V_{CPE5} , V_{CPE7} , where the voltage drop across each CPE is the sum of the product of the real impedance and the current, and the voltage drop related to the reactance (i.e., the capacitive element of CPE).

At every timestep, V_{OC} is expressed as a sixth order polynomial of the state of charge, SOC, where the empirical polynomial coefficients a_k are fitted against the experimental data at very low C-rate (0.05 C in this study) following regression analysis [39,40]. The SOC is a function of the maximum capacity, Q_{max} , of the battery which is adjusted with cycling, according to an artificial intelligence function that adjusts Q_{max} at cycle ic on the basis of the Q_{max} variation from the previous cycles obtained from historical experimental data.

3. Materials and Methods

2032 coin-cells were fabricated in the form of full (C-LFP) and half battery cells (C-Li and Li-LFP). Each cell was of an area of 1.77 cm^2 . The LFP cathode was a 60 mm thick coating of 80 wt% LFP (Hi Group, Korea), 15 wt% SuperP carbon (particle size $d_{50} = 40 \text{ nm}$, BET = $62 \text{ m}^2 \text{ g}^{-1}$, bulk density 160 kg m^{-3} , TIMCAL, Belgium) and 5 wt% binder on carbon-coated aluminium foil (MTI, US) as current collector. The C anode was a 30 mm thick coating of 90 wt% graphite (artificial graphite, particle size $d_{50} = 19\text{--}23 \text{ nm}$, tap density of $\geq 990 \text{ kg m}^{-3}$, BET $\leq 4.2 \text{ m}^2 \text{ g}^{-1}$ MTI, US), 5 wt% acetylene carbon black (average particle size 42 nm, specific surface area, BET = $75 \text{ m}^2 \text{ g}^{-1}$, bulk density $170\text{--}230 \text{ kg m}^{-3}$, Alfa Aesar, UK) and 5 wt% binder on carbon-coated copper foil (MTI, US) as current collector. For the half cells, the Li anode was in the form of foil (Sigma Aldrich, UK). The separator was a bilayer of a glass fiber (GF/F) filter and Celgard 3501. 300 ml of electrolyte 1 M LiPF_6 in ethylene carbonate/dimethyl carbonate EC/DMC 50:50 v/v (Sigma Aldrich, UK) was added in each cell. Three binders were investigated, all supplied in powder form: PVDF of MW = 534,000 (Sigma Aldrich, UK), KynarFlex[®] PVDF 2801-00 (Arkema, France) a PVDF copolymer of melting point $T_m = 143 \text{ }^\circ\text{C}$, and Kynar PowerFlex[®] LBG (Arkema, France) a semicrystalline, high molecular weight copolymer of vinyl F₂ of $T_m = 154 \text{ }^\circ\text{C}$.

Initially, LFP and graphite powders were dried separately in a static oven at 120 °C overnight to remove moisture from the sample. For the LFP electrodes, 12 g LFP powder and 2.25 g SuperP carbon powder were mixed and ground using an Agate mortar and pestle for 45 min. A slurry was prepared adding 55 mL solvent to this powder mixture and kept under magnetic stirring for 1 h [48]. Then the mixture was heated under magnetic stirring to evaporate the excess solvent, where a 10% solution of the required amount of binder was added in the last half-hour of stirring. The formed paste was coated onto the current collector foil using a dogbone-shaped coating tool at 60 mm gap, aiming for a 60 mm thick coating. The solvent was NMP for the PVDF binder and acetone for the two Kynar® binders. The LFP electrode coatings prepared using NMP as solvent were dried in a static oven at 80 °C overnight. The obtained electrodes were cut into 15 mm discs and dried in a vacuum oven at 120 °C for 2 h before transferring them to a glovebox. LFP electrode coatings prepared using acetone as solvent were dried at room temperature for two days to remove the solvent. Finally, all the prepared LFP electrodes were evacuated in the glovebox antechamber overnight to remove any remaining solvent/moisture from the electrode surface.

The preparation of the graphite electrode coating was similar. Mixtures in two separate glass containers, 9 g graphite added to 25 mL solvent and 0.5 acetylene carbon black added to 25 mL solvent, were prepared. Each mixture was sonicated in a bath for 30 min, followed by magnetic stirring for 30 min. 0.5 g binder was dissolved in 10 mL solvent. The two mixtures and binder solution were mixed and magnetically stirred for 1 h. Then the mixture was heated under magnetic stirring to evaporate the excess solvent and the paste was coated onto the current collector foil with the dogbone coating tool set at 30 mm gap, aiming at 30 mm thick coating. The graphite coatings with the KynarFlex® PVDF 2801-00 binder and the Kynar PowerFlex® LBG binder peeled easily off the current collector foil and it was not possible to be used in coin cell fabrication. As a result, anode coatings were investigated only with the PVDF binder.

Furthermore, wet adhesion tests were carried out for accelerated durability testing of the cathode coating with different binders. For each coating, 10 samples of 25 × 25 mm were soaked in the electrolyte solution EC/DMC for 12 h. Next, each sample was removed and cross-cuts were made with a sharp razor blade according to ASTM D3359-02 to create squares of about 7 × 7 mm each. The coatings were left to dry and the cut lines were first observed. Then an adhesive tape was smoothed over each square and was pulled off rapidly. The area portion removed by the adhesive tape in each square was then measured.

Overall, the electrode coatings were examined under the high-resolution scanning electron microscope HR-SEM JEOL-7100 F in SEM and EDX (energy dispersive X-ray analysis) mode before any testing (as prepared) and postmortem after 25 electrochemical test cycles. The cycled cells were disassembled in a glovebox under argon atmosphere, rinsed with dimethyl carbonate three times and then evacuated in the antechamber. Samples for postmortem SEM analysis were transferred in a sealed bag filled with argon gas.

XPS (X-ray photoelectron spectroscopy) was carried out using a Thermo Scientific K-Alpha⁺ XPS instrument. Spectra were obtained in constant analyzer energy mode with pass energies of 200 and 50 eV and a step size of 0.4 and 0.1 eV for survey and high-resolution spectra, respectively. A monochromated Al K α X-ray source was used with a 400- μ m radius spot. For data acquisition and analysis, Thermo Scientific Avantage V5.980 software was used. Transfer of samples from the glovebox to the spectrometer was achieved without exposure to the ambient atmosphere by the use of a Thermo Scientific Vacuum Transfer Module (VTM). This allows the postmortem samples to be prepared and mounted within the argon atmosphere of the glovebox. The VTM is then loaded into the entry lock of the K-Alpha⁺ spectrometer which is then pumped down in the usual manner. Once a high vacuum is achieved, the VTM is opened and the sample(s) are transferred to the analysis chamber for XPS.

The half and full battery cells were subjected to electrochemical testing using a Gamry Interface 1010E potentiostat. The electrochemical tests included electrochemical impedance

spectroscopy (EIS) in potentiostatic mode in the frequency range of 10 mHz–1 MHz; cyclic voltammetry (CV) at five different scan rates; and galvanostatic charge-discharge (GCD) cycling at 0.05 C.

4. Results

4.1. Experimental Results

After the cathode coatings with the different binders were prepared, they were first subjected to adhesion testing as a form of accelerated durability test. After they were soaked in the electrolyte solution for 12 h, they were cross-cut with examples of results presented in Figure S1A; the cuts in the coatings with PVDF binder and KynarFlex® PVDF 2801-00 binder are invisible in the images and in reality they were barely defined on the surface of the coating, never reaching the current collector foil; however, the cuts in the coating with Kynar PowerFlex® LBG binder are clearly visible all the way to the current collector foil, with a cut width of 0.8 ± 0.2 mm on average for all samples, indicating that the coating with this binder had weak wet scratch resistance. After stage B of the adhesion test (Figure S1B), it was found that the KynarFlex® PVDF 2801-00 binder induced excellent adhesion strength with only $1.0 \pm 0.5\%$ of the coating mass removed by the adhesion tape. This was not the case with the other two binders: the coating with the PVDF binder was the worst with $95 \pm 2\%$ of its mass removed, and the coating with the Kynar PowerFlex® LBG binder had $76 \pm 2\%$ of its mass removed by the adhesive tape.

Figure 2 presents the SEM micrographs of the LFP coatings with different binders, as prepared and postmortem after 25 electrochemical cycles of half cells. The images in Figure 2(a1,b1,c1) reveal the microstructure and degree of particle segregation in the LFP coatings, as prepared, which is quantified in the particle size distribution graphs in Figure 2d–f. The high resolution SEM images in Figure S2 reveal that particles of about 200–500 nm size in the coating with the PVDF binder are homogeneously dispersed with some small aggregates of about 1 mm size. Particle segregation is observed for the coating with the Kynar PowerFlex® LBG binder in Figure S2(c1), with aggregates of up to about 5 mm. The PSDs in Figure 2d–f. show that the coating with the PVDF binder has the greatest number of small particles, up to 10 mm diameter, compared to the other two Kynar copolymer binders. The PSDs also reveal that the coatings with the KynarFlex® PVDF 2801-00 binder and the Kynar PowerFlex® LBG binder have 73% and 14% more particles greater than 50 nm, respectively, than the coating with the PVDF binder, indicating particle segregation in the coatings with the Kynar copolymer binders. This is attributed to the sticky nature of the flexible component in the Kynar copolymers, as it was also proven from the adhesion test in which the PVDF binder created the worst adhesion in the coating. Some cracks are observed in the coating with the Kynar PowerFlex® LBG binder in Figure 2(c1), which can be attributed to the more brittle character of this highly crystalline binder. In fact, pin-holes were visible to the naked eye in this coating.

Postmortem characterization of the LFP coatings after battery cycling show flattened microstructures with original small gaps between particles now totally bridged with the formed SEI. More detail of the formed SEI around small particles in the higher magnification images is seen in Figure S2(A2,B2,C2) (postmortem) against Figure S2(A1,B1,C1) (as prepared). The PSDs in Figure 2d–f show clearly that the number of small microparticles is reduced in all postmortem coatings, as well as the specific surface area, especially for the coatings with the PVDF and the KynarFlex® PVDF 2801-00 binder. It must be noted that the information available in the PSDs and the SEM micrographs in Figure 2 covers only microparticles. Nanoparticles and cracks of nanosize width would increase the surface area available for the redox battery reactions.

XPS analysis was carried out for each binder with the results presented in Figures S3–S5: PVDF consists of 49.7 at% C (C1s at 286.4 eV), 50.1 at% F (F1s at 688.1 eV) and 0.2 at% O (O1s at 532.7 eV); KynarFlex® PVDF 2801-00 contains 47.7 at% C (C1 at 286.4 eV), 52 at% F (F1s at 688.2 eV) and 0.3 at% O (O1s at 533.8 eV); Kynar PowerFlex® LBG binder contains 53.2 at% C (C1s at 285 eV), 13.4 at% F (F1s at 688.5 eV) and 23.6 at% O (O1s at 532.1 eV).

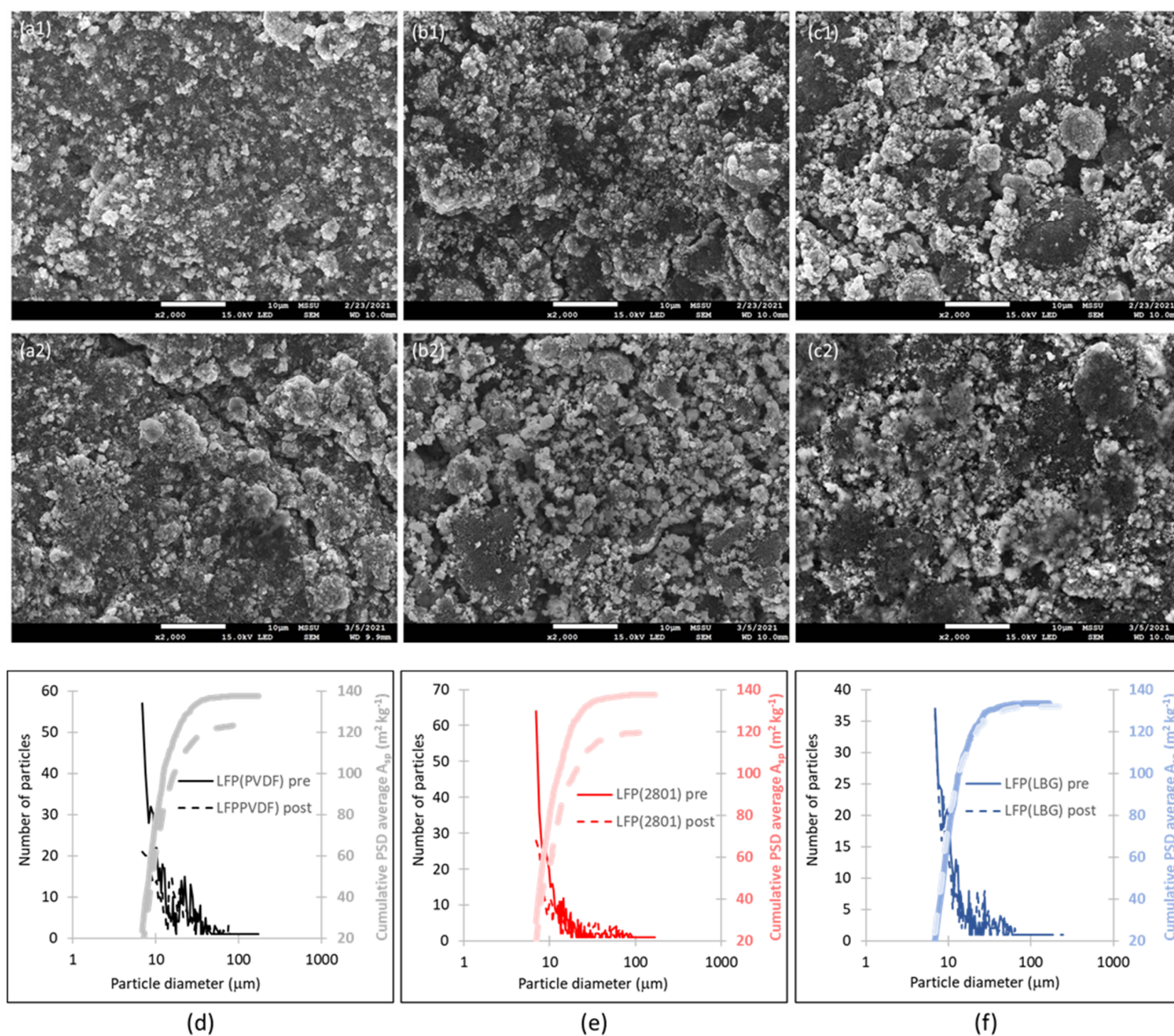


Figure 2. SEM micrographs of coatings as prepared (second index: 1) and postmortem after 25 battery cell cycles (second index: 2). First index: (a): PVDF binder; (b): KynarFlex® PVDF 2801-00 binder; (c): Kynar PowerFlex® LBG binder. Graphs of particle size distribution (PSD) of each coating ((d): with PVDF binder, (e) with KynarFlex® PVDF 2801-00 binder, (f) with Kynar PowerFlex® LBG binder) as prepared before any battery cycling (solid lines) and postmortem after 25 battery cycles (broken lines); in each graph, thin lines show PSDs in terms of number of particles on left hand side axis, and wide lines of lighter color show cumulative PSDs in terms of specific area on the right hand side axis.

Figures 3–5 present the XPS spectra of the surface of the LFP coating with different binders, as prepared (a1) and after 25 cycles of battery testing (a2). Figure 3 presents the XPS spectra of the surface of the LFP coating with the PVDF binder. The main C1s peak at 285 eV denotes the C–C bonds in PVDF and SuperP carbon which reduces substantially after battery cycling, possibly due to the SEI formation on top of the surface of the original LFP coating. There is also a second C1s peak at 291 eV characteristic of CF_2 in PVDF and the O=C–O group [49], which is possibly present in SuperP carbon. A peak around 55.4–55.9 eV in Table S1 represents the combination of the Fe3p and Li1s peaks, hence, it is very difficult to distinguish and determine the lithium concentration in the LFP cathode

from XPS. The Fe2p3/2 peak at 713 eV characteristic of FePO₄ is considerably reduced after cycling, attributed to thick SEI formation over the LFP coating, as XPS can detect surface features to very small depth of the order of 10 nm; for this reason, no Fe2p peak fit is produced for the cycled specimen (a2). Figure 3(a1) exhibits both P2p at 134 eV and P2s at 192 eV, which decreases in postmortem after battery cycling in Figure 3(a2) (in fact, the weak P2s peak disappears) due to the formation of the thick SEI layer. Given the dominance of the P2p over the P2s peak, XPS data quantification in Table S1 is based on the P2p peak. Further analysis of the P2p peak in Figure 3 denotes the P2p3/2 peak at 133.4 eV, characteristic of PO₄ in C_xH_y environment, present in coatings both before and after cycling, with the additional peak P2p at 137 eV characteristic of Li_xPF_yO_z in the LFP coating after 25 cycles, denoting a side reaction in the electrolyte with moisture or oxygen traces [50]. The O1s peak at 532 eV, characteristic of PO₄ but also in C–O, does not broaden after cycling as observed in previous studies of Li-LFP cells [51], but increases in intensity due to the oxygen of the electrolyte solvents. The F1s peak around 688 eV, indicating the PVDF binder, remains at the same position before and after cycling with a distinct shoulder at 684.9 eV after cycling, which is assigned to LiF [52]. Hence, the SEI seems to consist of a considerable amount of epoxide groups (C–O–C) and some Li_xPF_yO_z and LiF.

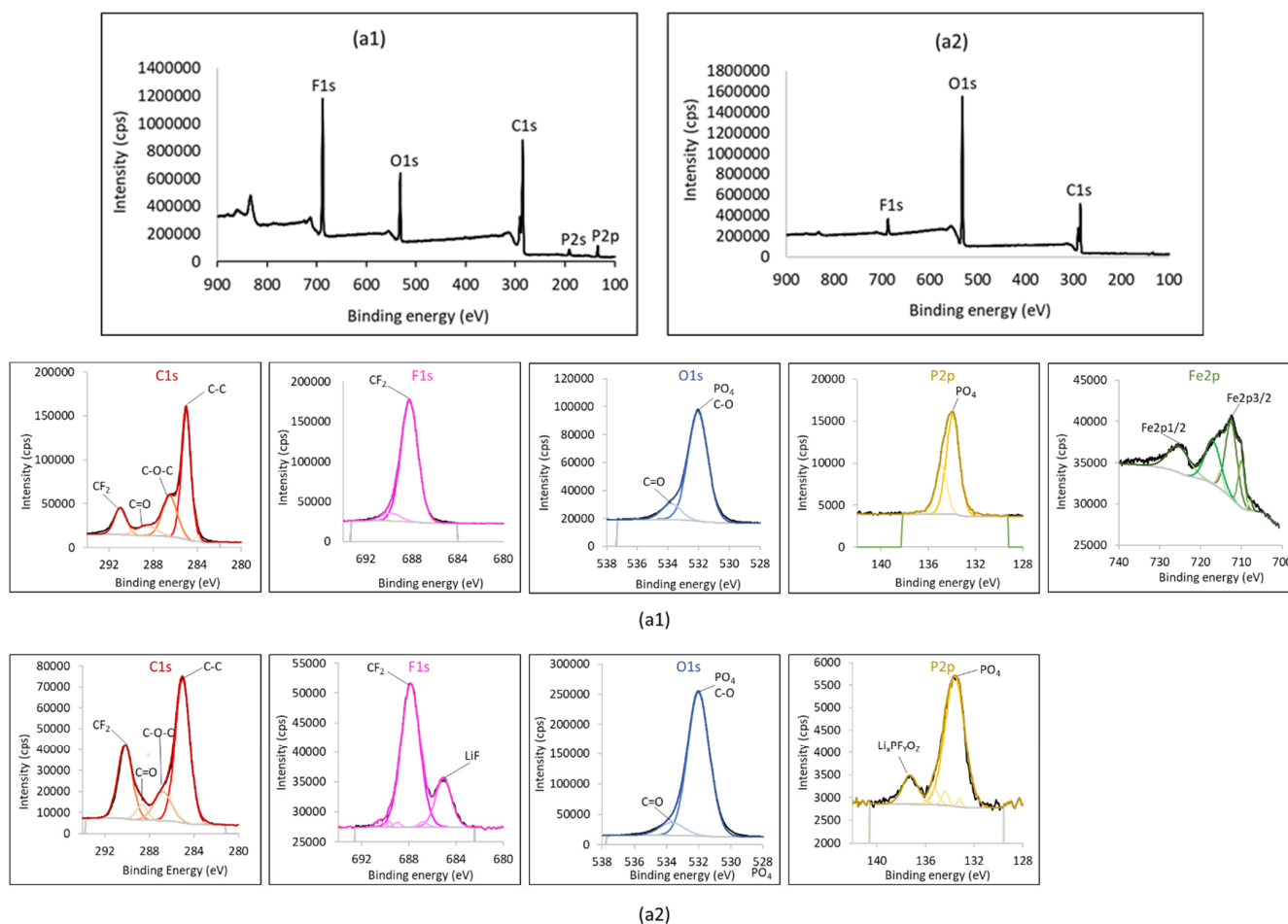


Figure 3. XPS spectra of the LFP cathode coating with PVDF binder: (a1) as prepared and (a2) post-mortem after 25 battery cell cycles.

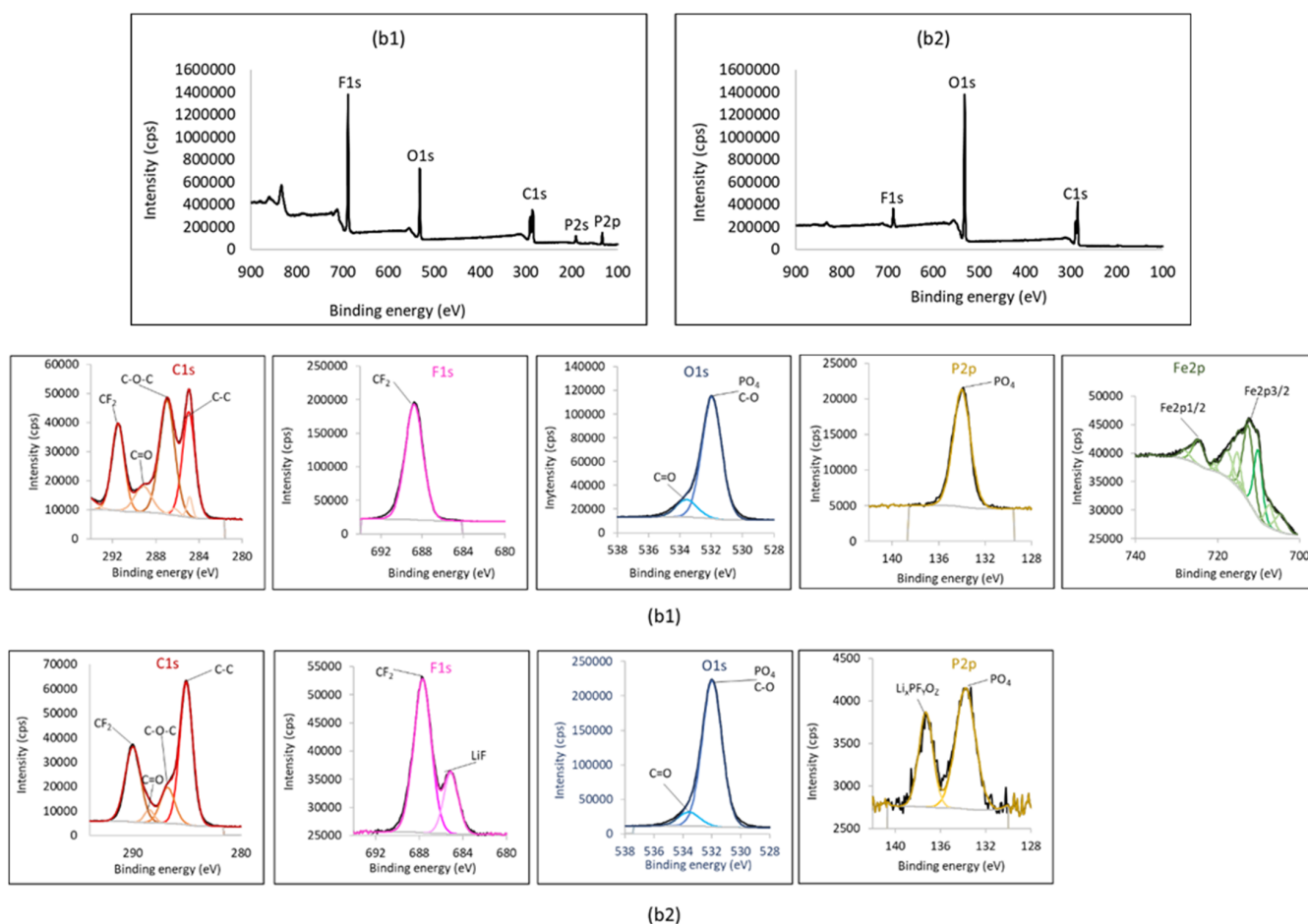


Figure 4. XPS spectra of the LFP cathode coating with KynarFlex[®] PVDF 2801-00 binder: (b1) as prepared and (b2) postmortem after 25 battery cell cycles.

Similar trends are observed for the LFP coatings with KynarFlex[®] PVDF 2801-00 and Kynar PowerFlex[®] LBG binders in Figures 4 and 5, respectively. The LFP coating with KynarFlex[®] PVDF 2801-00 contains a significant proportion of C–O–C groups before any cycling, as shown in the C1s spectrum in Figure 4, which is reduced after cell cycling. Tables S1–S3 present the XPS quantification data for the coatings with the three binders, demonstrating increased content of lithium (Li1s) and oxygen (O1s) after cell cycling, consistent with a formed SEI containing LiF, C–O–C groups and some $\text{Li}_x\text{PF}_y\text{O}_z$. Careful observation of all individual element peaks in Figures 3–5 reveals some shifts to lower energies after battery cycling, possibly uncovering the presence of more compounds on the SEI surface. More specifically: the C1s peak is at the same binding energy of 284.98 eV before and after cycling for the two coatings (Figures 3 and 4), but shifts to 284.88 eV postmortem for the coating with the Kynar PowerFlex[®] LBG binder in Figure 5; this indicates the addition of C–O–O functionality for this coating after battery cycling which may be attributed to alkyl carbonates (RCO_2OLi) originating from the decomposition of carbonate solvent by ring opening and polymerization. The C1s peak at 291.2 eV related to the CF_2 group in the binders is also shifted to lower energies of 289.9–290 eV after battery cycling for all coatings, which is also attributed to the presence of Li_2CO_3 generated from the decomposition of the carbonate solvents. The F1s peak moves from 688.1–688.8 eV to 687.3–687.8 eV after battery cycling for all coatings, which indicates ionic bonding of F with a metal and is attributed to the formation of LiF. The P2p peak is shifted from 133.88 eV to 133.58 (PVDF and KynarFlex[®] PVDF 2801-00 binders)–133.78 eV (Kynar PowerFlex[®] LBG binder) after battery cycling, indicating the presence of Li_xPF_y produced from the reduction of the electrolyte salt LiPF_6 to LiF and Li_xPF_y .

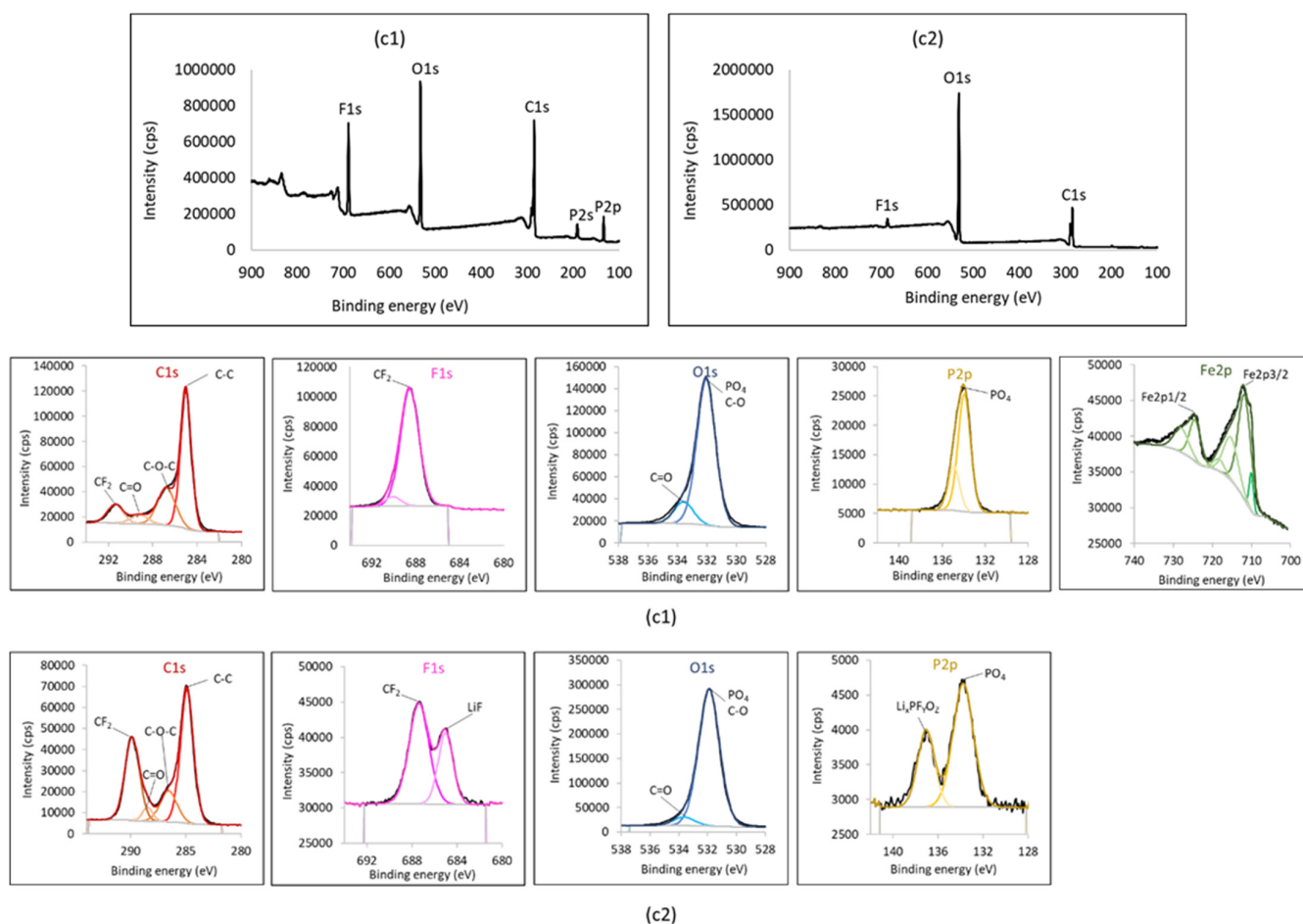


Figure 5. XPS spectra of the LFP cathode coating with Kynar PowerFlex[®] LBG binder: (c1) as prepared and (c2) postmortem after 25 battery cell cycles.

Finally, comparing the F1s peak in the coatings with the different binders, Figure 3(a1) and Figure 5(c1) reveal an additional small fitted peak at 690.2 eV and 690.85 eV, respectively, which after extensive search in the NIST XPS database were found to indicate CF₂-CF₂ segments from the binder for the PVDF and the Kynar PowerFlex[®] LBG binder; no such peak was fitted for the KynarFlex[®] PVDF 2801-00 binder (Figure 4(b1)). After battery cycling, this peak disappears in Figure 5(c2) for the coating with the Kynar PowerFlex[®] LBG binder, attributed to the fact that the binder is concealed under the thick SEI layer. However, Figure 3(a2) reveals that for the coating with the PVDF binder, after cycling, new small peaks are fitted at 690.6, 690.1, 688.9 and 687 eV, which correspond to CF₃, CF₂-CF₂, CH₂CHCOOCH₂CH₂(CF₂)_m(CF₃)_n and CHF-CH₂, respectively; the first and the two last groups indicate chemical changes in the PVDF binder in the presence of the electrolyte during the battery cycling.

Figure 6 presents SEM/EDX micrographs of the LFP coatings with different binders, as prepared, and postmortem after 25 electrochemical cycles of half-cells. This technique detects elements not just at the surface but deeper under the surface to about 1–2 μm, depending on element size. As a result, it goes deeper than just the surface microstructure displayed in Figure 2 and the PSDs before and after battery cycling in Figure 2 that indicate particle aggregation due SEI formation on the surface layer. It also goes deeper than the XPS analysis of just a surface layer of about 10 nm, consisting of the SEI after battery cycling. The element mapping from the EDX analysis reveals the microstructure of the LFP particles under the SEI layer, as well as elements from the SEI layer. For the PVDF and KynarFlex[®] PVDF 2801-00 binders, it can be seen that in the postmortem micrographs Fe and F from LFP are evenly distributed at the micron level, and O seems more micro-fragmented after

25 cycles of Li^+ ion intercalation and deintercalation, indicating that LFP particles are expanded possibly due to Li^+ ion insertion, while the bridging of small interparticle gaps observed in the SEM images of Figure 3 might be due to this LFP particle expansion and filling and covering of the gaps with the SEI layer. Kynar PowerFlex[®] LBG binder, involved in particle agglomeration in the as prepared electrode, provides an even distribution of Fe in Figure 3(c1), before any cycling, so it is difficult to observe the cycling effects on the Fe EDX map. However, micro-fragmentation can be observed in the O and F EDX maps of the postmortem sample in Figure 3(c2) for this binder as well.

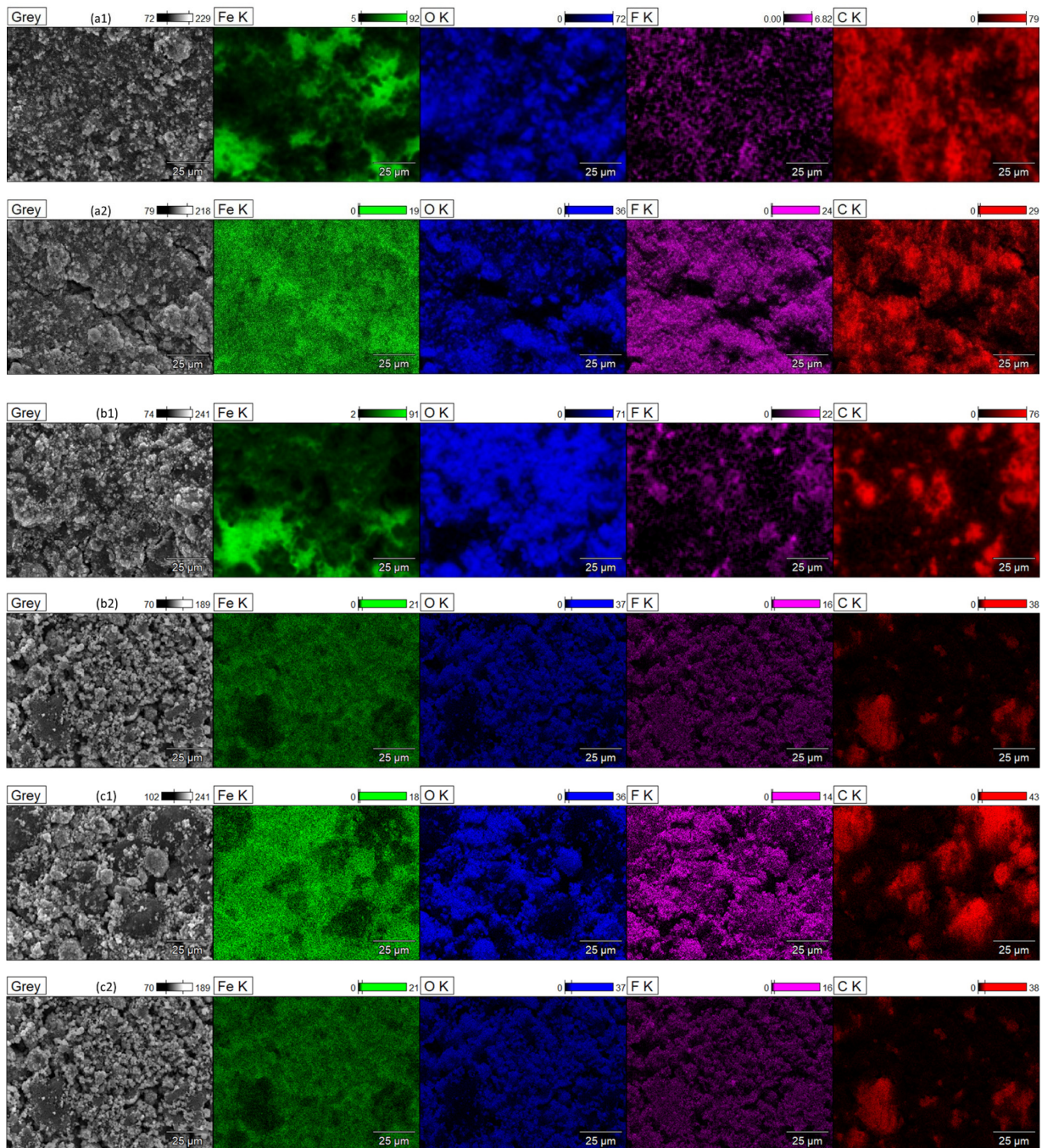


Figure 6. SEM/EDX maps (15 kV) of coatings as prepared (second index: 1) and postmortem after 25 battery cell cycles (second index: 2). First index: (a): PVDF binder; (b): KynarFlex[®] PVDF 2801-00 binder; (c): Kynar PowerFlex[®] LBG binder.

Figure 7 presents the Nyquist plots from the EIS tests of the Li-LFP battery cells as fabricated and pre-cycled. It is thought that differences between the ESR (equivalent in series resistance) values between the cathodes with different binders are due primarily to the different loading of the LFP coatings. Differences in the electrochemical double layer (EDL) capacitance ($1/Z_{im}$ at the lowest frequency) are also observed between the different LFP coatings, with the LFP coating with the PVDF binder exhibiting the lowest EDL capacitance. It seems that particle aggregation in the LFP coatings with either of the two Kynar[®] binders, observed in the SEM images in Figure 2, reduces the micropore size which enhances the EDL capacitance for the small Li^+ ions [28,29] as it has been established that the highest EDL capacitance is achieved when the micropores are close to the size of the electrolyte ions.

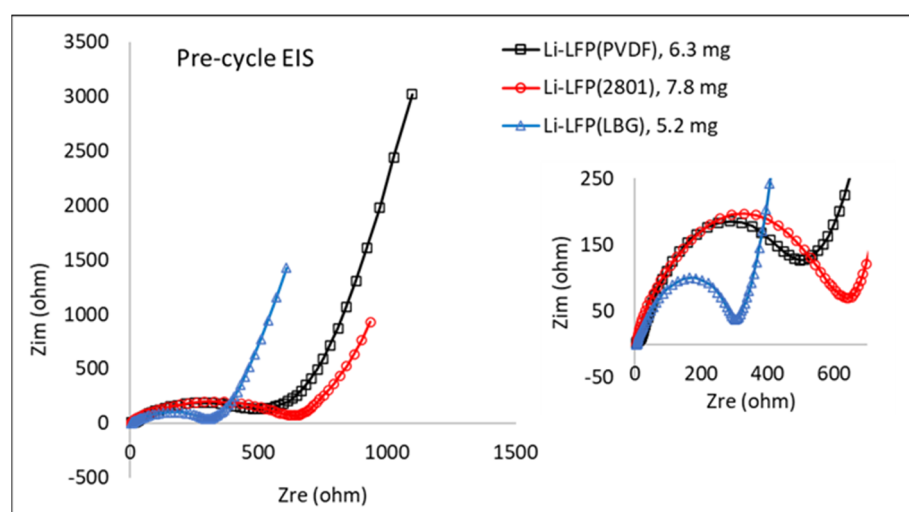


Figure 7. Nyquist plots from EIS tests of Li-LFP battery cells, after they have been fabricated and before any cycling, for LFP cathodes with different binders (PVDF binder; KynarFlex[®] PVDF 2801-00 binder; Kynar PowerFlex[®] LBG binder); the legend of each curve also gives the mass of the LFP coating (including additives).

Figure 8 presents the results of the GCD tests for the Li-LFP cells for the three different binders in the LFP coating. All cells present a discharge capacity of 152 ± 1 mAh/g_{LFP}. The LFP cathode with the PVDF binder exhibits the flattest plateau in both charge and discharge, indicating the lowest resistance in Li^+ ion diffusion. Apart from the higher ion resistance in the LFP coatings with the other two binders, these also show lower coulombic efficiency between charge and discharge than the LFP coating with the PVDF binder.

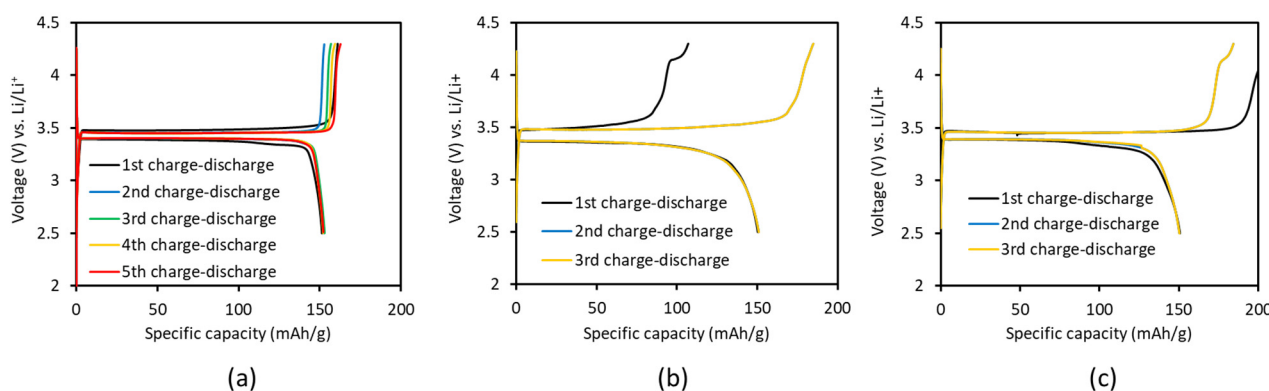


Figure 8. GCD test plots at 0.05 C for Li-LFP battery cells. Cathodes: (a) PVDF binder; (b) KynarFlex[®] PVDF 2801-00 binder; (c) Kynar PowerFlex[®] LBG binder.

CV tests were carried out in half cells at different scan rates and the results were used to determine the diffusion coefficient of Li^+ ions, D_{Li^+} , in the electrode, employing the Rendles-Shevchik equation [53]:

$$I_{\text{peak}} = 2.69 \times 10^5 n^{1.5} A D_{\text{Li}^+}^{0.5} r^{0.5} c \quad (20)$$

where I_{peak} is the peak current (A) in the voltammogram, n is the number of electrons in the electrochemical process, A is the electrode area (cm^2), r is the CV rate (V s^{-1}) and c is the initial concentration of Li^+ in the anodic process and of the vacancies in intercalates in the cathodic process (mol cm^{-3}). It has been suggested [53] that the specific surface area of LFP particles may be given by the following relation, as a function of the particle radius, R_p , and density $\rho = 3600 \text{ kg m}^{-3}$:

$$A_{\text{sp}} = \frac{3}{R_p \rho} \quad (21)$$

A mean LFP particle diameter of 450 nm was estimated from the SEM micrographs in this study, yielding $A_{\text{sp}} = 3700 \text{ m}^2 \text{ kg}^{-1}$. Figure 9a presents CV graphs for a Li-LFP cell with PVDF binder in the cathode and the linear fits of the Rendles-Shevchik equation to a correlation factor $R^2 = 0.998$. Considering the initial concentration of Li^+ ions in the cathode: $c_{\text{Li}^+} = 0.02282 \text{ mol cm}^{-3}$ and the same A_{sp} value as cycling progresses, the anodic process fit yields the anodic diffusion coefficient values: $D_{\text{Li}^+, \text{anodic}} = 2.02 \times 10^{-14}$ (6th cycle), 1.98×10^{-14} (7th cycle), 1.92×10^{-14} (8th cycle) $\text{cm}^2 \text{ s}^{-1}$, describing the rate of deintercalation of Li^+ ions from LFP. Assuming the same concentration $c = 0.02282 \text{ mol cm}^{-3}$, the cathodic process fit yield the cathodic diffusion coefficient values: $D_{\text{Li}^+, \text{cathodic}} = 1.26 \times 10^{-14}$ (6th cycle), 1.21×10^{-14} (7th cycle), 1.24×10^{-14} (8th cycle) $\text{cm}^2 \text{ s}^{-1}$, which are about 60% of the $D_{\text{Li}^+, \text{anodic}}$ values. Our anodic diffusivity values are in total agreement with Galaguz et al. [53] and our cathodic diffusivity values are higher than theirs, where their $D_{\text{Li}^+, \text{cathodic}}$ values are 50% of their $D_{\text{Li}^+, \text{anodic}}$ values [53]. In general, it is evident that our cathodic I_{peak} values in the intercalation process and the corresponding gradient are 79% lower than our anodic I_{peak} values and gradient, possibly due to (a) the smaller number of vacancies during intercalation compared to the number of Li^+ ions in the cathode for deintercalation and (b) lower diffusion coefficient during intercalation compared to the easier deintercalation process. This results in inefficiency between charge and discharge.

The CV results for the Li-LFP half cell with cathode binder KynarFlex[®] PVDF 2801-00 binder are presented in Figure 9b. Clearly, the CV displays wide peaks indicating a highly controlled cycle by diffusion, with additional evidence of the higher resistance for this cell with this cathode binder (Figure 7) in the anodic step. The CV plots display a wider difference of anodic-cathodic potential peaks for Li-LFP(2801), $DE_o = 0.43 \text{ V}$ at 0.03 mV s^{-1} and 0.85 V at 0.14 mV s^{-1} , compared to $DE_o = 0.23 \text{ V}$ at 0.03 mV s^{-1} and 0.40 V at 0.14 mV s^{-1} for Li-LFP(PVDF), consistent with a more diffusion-controlled process for Li-LFP(2801). The linear fits of the Rendles-Shevchik equation produced lower gradient values for Li-LFP(2801) (correlation factor $R^2 = 0.971$) than for Li-LFP(PVDF), which further yielded a much lower diffusion coefficient for Li-LFP(2801): $D_{\text{Li}^+, \text{anodic}} = 1.39 \times 10^{-15} \text{ cm}^2 \text{ s}^{-1}$ (three cycle average) and $D_{\text{Li}^+, \text{cathodic}} = 0.88 \times 10^{-15} \text{ cm}^2 \text{ s}^{-1}$ (three cycle average), with the cathodic value also about 60% of the anodic value.

Figure 9c presents the CV plots for the Li-LFP half-cell with Kynar PowerFlex[®] LBG binder in the cathode. Sharp peaks are encountered with difference of anodic-cathodic potential peaks: $DE_o = 0.23 \text{ V}$ at 0.03 mV s^{-1} and 0.41 V at 0.14 mV s^{-1} , similar to that of the Li-LFP(PVDF) half-cell. The determined diffusion coefficients from the linear fits of the Rendles-Shevchik equation (correlation factor $R^2 = 0.993$) for the Li-LFP(LBG) half-cell are: $D_{\text{Li}^+, \text{anodic}} = 2.65 \times 10^{-14} \text{ cm}^2 \text{ s}^{-1}$ (three cycle average) and $D_{\text{Li}^+, \text{cathodic}} = 1.39 \times 10^{-14} \text{ cm}^2 \text{ s}^{-1}$ (three cycle average), with the cathodic value 52% of the anodic value. These diffusion coefficient values for the Li-LFP(LBG) half-cell are higher than those of the Li-LFP(PVDF) half-cell.

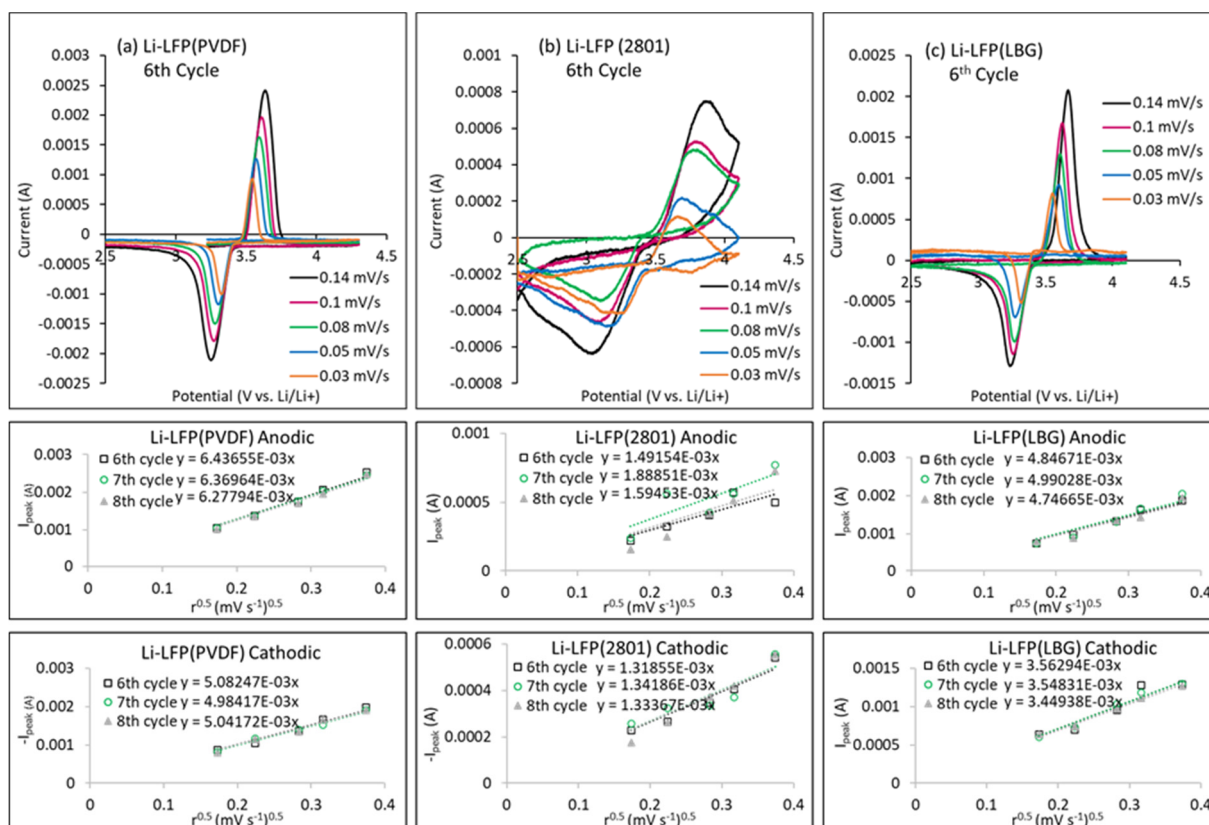


Figure 9. CV plots from CV cycling of Li-LFP battery cells and the linear fits of the Rendles-Shevchik equation for determining the Li^+ ion diffusion coefficient in cathode. Cathodes: (a) PVDF binder; (b) KynarFlex® PVDF 2801-00 binder; (c) Kynar PowerFlex® LBG binder.

Figure S6 presents the results from the EIS and GCD electrochemical tests of the graphite-Li half cells. A discharge capacity of $310 \text{ mAh/g}_{\text{graphite}}$ was measured in GCD tests at 0.05 C. Figure S7 presents CV plots for the graphite-Li half cells at different rates. All peaks are below 0.2 V in discharge which means that they correspond to lithium intercalation and SEI formation only, where peaks at higher voltages would indicate SEI formation due to the electrolyte (0.3–0.9 V) or SEI formation due to additives (1–1.4 V) [54]. The CV plot demonstrates multi-stage transitions [55–57] during the lithiation and delithiation of graphite that have been grouped to three oxidation (in charge) and three or four (at low voltage scan rate) reduction current peaks (in discharge). Table S4 presents the voltage values of these peaks identified from the voltage plateaus in the GCD curves in Figure S6.

Figure S8 presents the linear fits of the Rendles-Shevchik equation for all anodic and cathodic peaks of the CV plots of the graphite-Li half cells. Figure S8a shows that the fit equation for P_{01} has an intercept that indicates a systematic error in the determination of the baseline for all scan rates for this peak, which is the last peak at the highest voltage during the charge phase. No such issue is encountered for the rest of the oxidation and reduction peaks in Figure S8. Considering Equation (21), a mean graphite particle diameter of 21 nm and the graphite density of 2260 kg m^{-3} , a graphite specific area $A_{sp} = 126 \text{ m}^2 \text{ kg}^{-1}$ is estimated for the graphite anode. A mean lithium concentration of $0.0314 \text{ mol cm}^{-3}$ is assumed in the graphite anode, corresponding to the mean state of LiC_6 , to calculate the diffusion coefficient of Li^+ ions in graphite using the Rendles-Shevchik Equation (20). Table S5 presents the determined values of the diffusion coefficient for the three oxidation (intercalation) peaks and the four reduction (deintercalation) peaks. For peaks 1 and 2, the Li^+ ion diffusion seems faster during intercalation than in deintercalation, with particularly slow deintercalation for the P_{T1} peak.

4.2. Simulation Results

Figure 10a–e present the results of the computer simulations employing the SP model and their comparison with experimental data from the GCD tests. In some preliminary parametric simulation studies, it was observed that the higher are the ion diffusion coefficient and the surface area of the electrode, the higher is the capacity. All the diffusion coefficient values inputted in the simulations were the same as the values derived from the experimental CV data in Section 4.1. Figure 10a–c presents the results for the Li-LFP half cells for different cathode binders. To ensure a good fit between predictions and the experimental data of GCD tests, a 30(charge)–35% (discharge) higher S_p value was inputted in the simulations than what was assumed in Section 4.1 for the Li-LFP half-cell of cathodes with a KynarFlex[®] PVDF 2801-00 binder; this is attributed to the fragmentation of LFP cathode during cycling, which, although it would contribute to an increased capacity, might also increase the cathode resistance. A second order relation of cell resistance against SOC (or 1-SOC) was needed to fit the GCD curves at the end of each GCD stage for cathodes with KynarFlex[®] PVDF 2801-00 binder and Kynar PowerFlex[®] LBG binder. On the other hand, the surface area of the cathode of the Li-LFP(LBG) half-cell had to be reduced by 34 (charge)–42% (discharge) to fit the experimental GCD capacity, which can be attributed to the large degree of aggregates exhibited in the LFP(LBG) coating after preparation (Figure 6(c1)). Similar treatment had to be applied in the simulation of the Li-LFP(PVDF) half-cell, where the surface area of the cathode had to be reduced by 23 (charge)–27% (discharge) to obtain a good fit between predictions and experiment, although the resistance was independent of the SOC for this particular cell that exhibits approximately a flat potential curve during the GCD cycle. Figure 10d presents the results for the graphite-Li half-cell. The value for the graphite area inputted in the simulations was the same as the area value used for the fitting of the CV peaks in Section 4.1. The cathodic values for the four diffusion coefficients covering multistage transitions in the anode and presented in Table S5 were inputted in the simulations for both the charge and discharge phase and yielded the simulation lines presented in Figure 10d, which is in good agreement with the experimental data.

Finally, using the same input parameters for the anode and cathode as those used in the half cells, the GCD cycle of a full graphite-LFP battery cell was simulated employing the SP model, and the results are presented in Figure 10e together with the experimental data of five GCD cycles. It can be seen that the simulated GCD curves have a higher capacity than the experimental curves, apart from the first experimental charge curve which exhibits a long capacity as expected, which is associated with the formation of the SEI layer primarily on the graphite anode. The capacity of the experimental graphite-LFP cell in Figure 10e was limited by the mass of the LFP in the cathode. During discharge, given the limited mass of lithium intercalating the anode, it was considered that no large influx of Li^+ ions would occur in the cathode and, hence, it was assumed that no fragmentation of the cathode would take place: therefore, the S_p value was not increased in the simulation model for the full cell in Figure 10e (unlikely the simulation model in Figure 10b for the half cell). The lower capacity of the experimental data compared to the SP model predictions in Figure 10e and slow capacity reduction with cycling are attributed to clogging of the pores due to byproducts from electrolyte reactions, reduction of the diffusion coefficients of the electrodes and diminishing of the Li^+ ion supply. The latter is a serious problem for the graphite-LFP cells, whereas this was not the case for half cells which had an abundant reservoir of pure lithium.

The next step was to proceed with GCD simulations of the graphite-LFP battery cell using the EEC model. Figure 11a,b depict the fitting of the EEC model against the experimental EIS data before cell cycling and after 5 GCD cycles, respectively. It is clear the pre-cycling Nyquist plot presents only the typical contact resistance between electrodes and the current collector, whereas after cycling there is a substantial addition of a shoulder indicating the formed SEI. Table S6 presents the values of the fitted parameters of the EECM, pre-cycling and after 5 GCD cycles. R1 and R3 reduced after cycling, possibly due to better electrolyte wetting and improvement of one of the two electrode/current collector

interfaces. R2 remains the same before and after cycling. For VCE3, R4 almost doubles while CPE4 becomes more resistive after cycling, indicating increased resistance to ion diffusion after cycling, while also the pore surface is decreased, reducing the capacitance of CPE3. The new EECM feature after cycling is the emergence of the VCE4, with a huge R5 resistance but also considerable capacitance in CPE5: this new feature is attributed to the formation of SEI on the anode side with large resistance to ion transport but also considerable pore surface area to generate capacitance in CPE5.

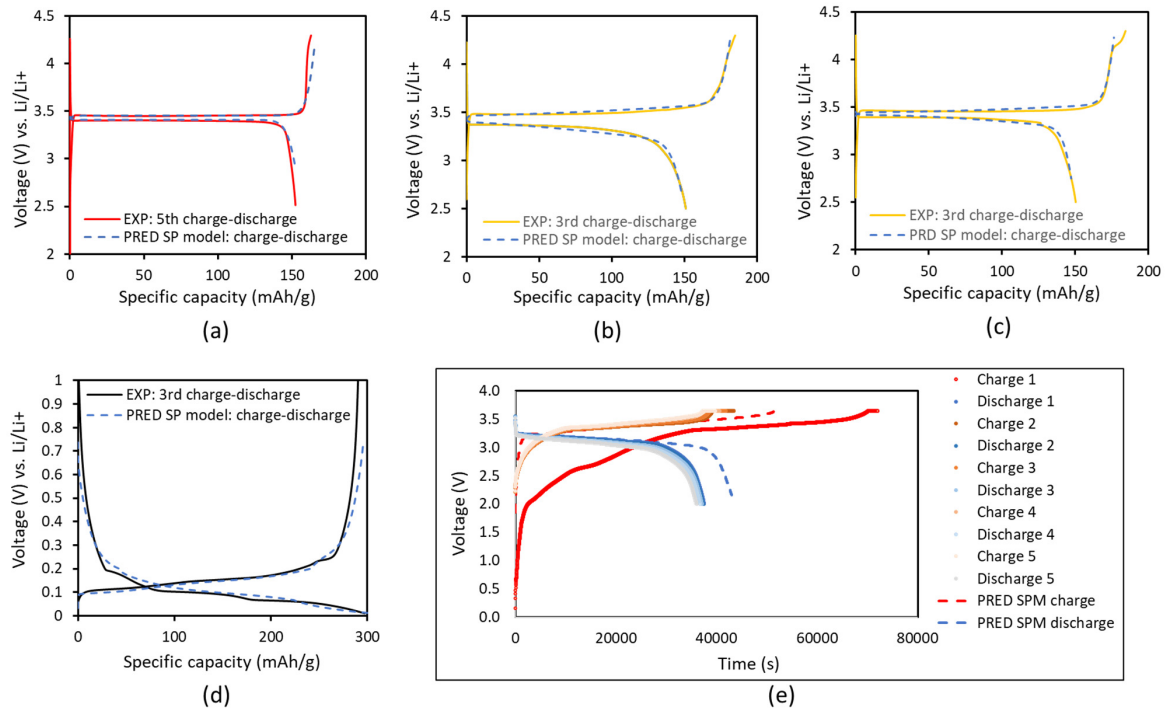


Figure 10. Plots of GCD results at 0.05 C, including predictions (PRED) from computational simulations using the SP model (broken lines) and experimental data (solid lines): (a) Li-LFP half-cell with PVDF binder in the cathode; (b) Li-LFP half-cell with KynarFlex® PVDF 2801-00 binder in the cathode; (c) Li-LFP half-cell with Kynar PowerFlex® LBG binder in the cathode; (d) graphite-Li half-cell with PVDF binder in the anode; (e) graphite-LFP battery cell with Kynar PowerFlex® LBG binder in the cathode and PVDF binder in the anode.

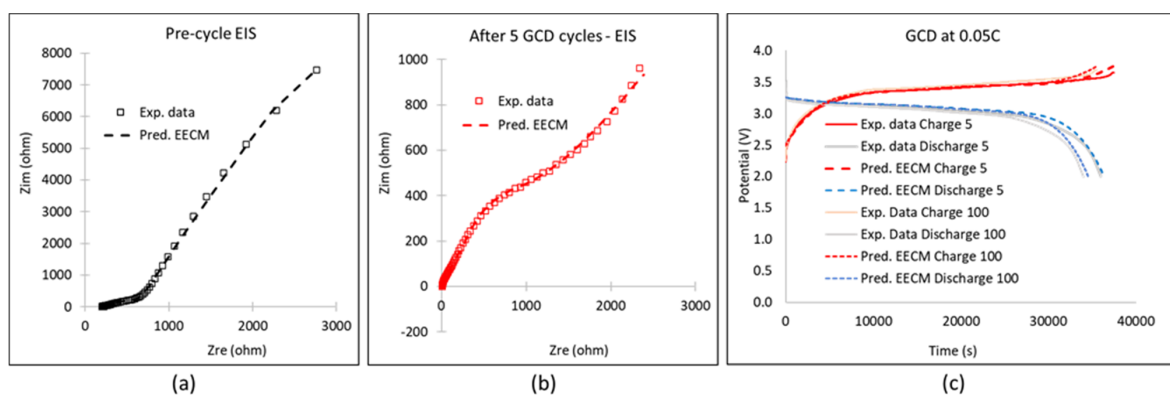


Figure 11. Comparisons of the predictions applying the EEC model (EECM) with experimental data from the testing of a graphite-LFP cell (with KynarFlex® PVDF 2801-00 binder in the cathode): (a) Nyquist plot showing the fit of the EEC model with the pre-cycling EIS data; (b) Nyquist plot showing the fit of the EEC model with the EIS data after five GCD cycles; (c) comparison between predictions of the EEC model and experimental data for the fifth and 100th GCD cycle at 0.05 C.

Figure 11c displays the comparison between the predictions of the EECM and the experimental data for the fifth GCD cycle of the graphite-LFP battery cell, where the EECM parameters were the same as those determined from the fit of the Nyquist plot in Figure 11b and the maximum capacity for the fifth cycle was adjusted according to the trend of the historical experimental data for GCD cycles one to four. It can be seen that the agreement between the predictions and the experimental data is much better for the EEC model (Figure 11c) than for the SP model (Figure 10e). Further to this, the experimental GCD cycling of the graphite-LFP battery cells was continued to 100 cycles with the data presented in Figure 11c. The battery capacity values as a function of cycle number were fit to a logarithmic relation up to the 50th cycle, as presented in Figure S9. This relation was then used in the EECM to predict the battery performance for the 100th cycle, while the rest of the parameters of the EEC model were maintained the same as in the fit of Figure 11b, assuming that the SEI does not change much after the fifth cycle. The predictions for the 100th cycle are presented in Figure 11c and are not that far from the corresponding experimental data, apart from the shape of the curve turning to the final voltage towards the end of the charge or discharge cycle indicating increased resistance in final ion diffusion.

5. Discussion and Concluding Remarks

A comprehensive study of LFP batteries has been presented, including electrochemical testing of half and full cells, microstructural images and surface composition maps and overall data for the cathodes for coatings as prepared (pre-cycling) and postmortem after 25 cycles, determination of the diffusion coefficients in the different redox processes in the cathode and anode from CV plots, and battery cell simulations using the SP model and the EEC model.

Three different binders were investigated for the cathode, where the KynarFlex[®] PVDF 2801-00 binder and the Kynar PowerFlex[®] LBG binder were explored, as they could be dissolved in acetone, which is a solvent with a much lower boiling point than NMP, the usual solvent for the PVDF binder. In an accelerated durability assessment of the cathode coatings via wet adhesion tests it was found that the coating with the KynarFlex[®] PVDF 2801-00 binder has excellent adhesion strength, the next best is that with the Kynar PowerFlex[®] LBG binder, and the worst is that with the PVDF binder. In terms of scratch resistance, the worst cathode coating is that with the Kynar PowerFlex[®] LBG binder, while the other two binders induce excellent scratch resistance. As a result of the adhesion properties, it was found that cathode particle aggregation was easier in cathode fabrication when using either of the two Kynar[®] binders compared to PVDF, with the latter exhibiting a large number of nano and small microparticles due to its poor adhesion properties which discourage particle aggregation. On the other hand, EIS and CV tests revealed that the cathode with the KynarFlex[®] PVDF 2801-00 binder had the highest resistance and the lowest Li⁺ ion diffusion coefficient attributed to the sticky, insulating copolymer. The cathode with PVDF binder had the highest Li⁺ ion diffusion coefficient attributed to the open channels left free by PVDF, which does not stick so well on the LFP particles as the Kynar copolymers. Hence, it seems that the LFP cathode with the PVDF binder favors ion diffusion and presents the flattest voltage plateau to the end of the charge and discharge phase in the GCD cycles of half-cells in the initial cycles. However, in a heavy-duty battery, possibly also with the production of gas after thousands of cycles, the PVDF binder would run the risk of coating delamination from the current collector, increasing the contact resistance and ultimately shortening the battery lifetime.

Postmortem characterization of cathodes revealed the expected phenomena associated with battery aging that was also encountered in previous studies [11,12]: pore clogging due to the formation of SEI (in all cathodes with either of the three binders) including Li_xPF_yO_z due to side reactions of electrolyte with traces of moisture or oxygen, LiF and Li_xPF_y due to the reduction of the electrolyte salt LiPF₆, epoxide groups from RCO₂OLi and Li₂CO₃ due to the decomposition of the carbonate solvents, and surface cracking and fragmentation. Graphite-Li half cells exhibited multistage transitions corresponding to

lithium intercalation and SEI formation, which was also observed and analyzed in several studies in the literature [55–57]. The full graphite-LFP cell demonstrated lower capacity than the half-cell capacity, which has been attributed to the loss of active Li^+ material [11] that could not be replaced from a large reservoir, as with the Li electrode reservoir of the half cells.

In modeling the battery cells, at first a simple SP model was employed to study the physicochemical processes in the battery cells, with the emphasis of Li-ion diffusion for which data were provided from the fitting of CV graphs using the Rendles-Shevchik equation for both anode (with PVDF binder) and cathode electrodes with all three binders. The further adjustments of the cathode surface area in the SP model simulations for the predictions to fit the experimental data provide additional insight of pore clogging due to SEI formation (surface area decreased) or particle fragmentation (surface area increased). In this manner, the SP model simulations contribute to the understanding of some aging effects during battery cycling. However, the simple SP model was unable to replicate the GCD curves of the full cell from the input data derived from the half cells. Furthermore, it would be rather complex to adjust the active area of cathode and anode, and the diffusion coefficients as a function of the number of cycles, in order to predict future battery cell behavior and lifetime using the SP model. As a result, the SP model is recommended for the study of specific physicochemical effects and would be easier to fit its parameters for a half cell.

On the other hand, the EEC model proved much easier to adapt, with fewer parameters to adjust as a function of the number of cycles on the basis of historical data of cell testing. This and the good agreement between EECM predictions with the experimental data of a “future” GCD cycle of a full graphite-LFP battery cell offer great promise for the EEC model to be able to forecast future battery behavior and the lifetime of batteries. This is used for batteries in transport applications, the grid, or consumer goods, so that the replacement time of a battery or the remaining time of a recycled battery can be predicted. Furthermore, the EEC model can be employed in the energy management of batteries, for example to establish an optimized schedule for battery charge and operation depending on the predicted battery state-of-health. Still, the modeling approach proposed in this study to predict future behavior and the lifetime of a Li-ion battery is based on the known cycling history of the battery. Therefore, our recommendation is to equip each battery with the memory storage of its operational history.

Supplementary Materials: The following are available online at <https://www.mdpi.com/article/10.3390/en15072332/s1>, Figure S1. Results of wet adhesion test of some of the samples of LFP coatings with different types of binders: PVDF binder; B: KynarFlex[®] PVDF 2801-00 binder; C: Kynar PowerFlex[®] LBG binder.; Figure S2. High magnification SEM micrographs of LFP coatings as prepared (second index: 1) and postmortem after 25 battery cell cycles (second index: 2). First index: A: PVDF binder; B: KynarFlex[®] PVDF 2801-00 binder; C: Kynar PowerFlex[®] LBG binder.; Figure S3. XPS data for the PVDF binder.; Figure S4. XPS data for the KynarFlex[®] PVDF 2801-00 binder.; Figure S5. XPS data for the Kynar PowerFlex[®] LBG binder.; Figure S6. Nyquist plot from the EIS test and results of the GCD tests of graphite-Li half cells.; Figure S7. CV plots at different scan rates (3 cycles) of graphite-Li half cells, with the three oxidation peaks during charge and the 4 reduction peaks during discharge annotated on the first plot.; Figure S8. The linear fits of the Rendles-Shevchik equation for determining the Li^+ ion diffusion coefficient in the graphite anode for the three oxidation peaks and the four reduction peaks of the CV plots in Figure S6.; Figure S9. Experimental data of maximum SOC of graphite-LFP battery cell as a function of cycle number (orange solid line: up to 50 cycles, blue solid lines to 100 cycles) and fit of the experimental data up to 50 cycles (orange broken line with the equation displayed on the graph). Table S1. XPS quantification data for coating of LFP with PVDF binder.; Table S2. XPS quantification data for coating of LFP with KynarFlex[®] PVDF 2801-00 binder.; Table S3. XPS quantification data for coating of LFP with Kynar PowerFlex[®] LBG binder.; Table S4. Oxidation (charge) and reduction (discharge) plateau voltages from the GCD cycles of graphite-Li half cells.; Table S5. Diffusion coefficient of the Li^+ ions in the graphite anode, determined using the Rendles-Shevchik equation and the gradient of the linear fits

in Figure S7 (average of 3 cycles); Table S6. Fitted parameters of the EECM against experimental EIS data, pre-cycling and after 5 GCD cycles of a graph-ite-LFP cell.

Author Contributions: Conceptualization, C.L.; methodology, all; software, C.L., M.D. and E.H.N.; validation, J.P.B., E.H.N. and C.L.; formal analysis, J.P.B., E.H.N., C.L. and S.J.H.; investigation, J.P.B., M.A.Y., M.D., E.H.N., C.L., S.J.H. and J.F.W.; resources, C.L., R.S. and J.F.W.; data curation, J.P.B. and C.L.; writing—original draft preparation, J.P.B., M.D. and C.L.; writing—review J.P.B., C.L. and J.F.W.; visualization, J.P.B., C.L. and S.J.H.; supervision, C.L., R.S. and J.F.W.; project administration, C.L.; funding acquisition, C.L. All authors have read and agreed to the published version of the manuscript.

Funding: The University of Surrey authors gratefully acknowledge funding of this study by EPSRC under the HiPoBat project: ISCF Wave 1: High Power Material Hybridised Battery, EP/R022852/1.

Institutional Review Board Statement: Not applicable.

Informed Consent Statement: Not applicable.

Data Availability Statement: Apart from the data provided at Supplementary Material, further data associated with the experimental results will be provided after reasonable requests.

Acknowledgments: The authors gratefully acknowledge the use of facilities of the Microstructural Studies Unit (MSSU) at the University of Surrey.

Conflicts of Interest: The authors declare that they have no conflict of interest.

References

1. Chen, Y.; Kang, Y.; Zhao, Y.; Wang, L.; Liu, J.; Li, Y.; Liang, Z.; He, X.; Li, X.; Tavajohi, N.; et al. A review of lithium-ion battery safety concerns: The issues, strategies, and testing standards. *J. Energy Chem.* **2021**, *59*, 83–99. [[CrossRef](#)]
2. Saleh, A.; Lekakou, C.; Doherty, J. An investigation into energy harvesting and storage to power a more electric regional aircraft. *Adv. Aircr. Spacecr. Sci.* **2021**, *8*, 17–30.
3. Santucci, A.; Sornioti, A.; Lekakou, C. Power split strategies for hybrid energy storage systems for vehicular applications. *J. Power Sources* **2014**, *258*, 395–407. [[CrossRef](#)]
4. Lei, C.; Fields, R.; Wilson, P.; Lekakou, C.; Amini, N.; Tennison, S.; Perry, J.; Gosso, M.; Martorana, B. Development and evaluation of a composite supercapacitor-based 12 V transient start–stop power system for vehicles: Modelling, design and fabrication scaling up. *Proc. Inst. Mech. Eng. Part A J. Power Energy* **2021**, *235*, 914–927. [[CrossRef](#)]
5. Reece, R.; Lekakou, C.; Smith, P.A. A high-performance structural supercapacitor. *ACS Appl. Mater. Interfaces* **2020**, *12*, 25683–25692. [[CrossRef](#)]
6. Lei, C.; Lekakou, C. Activated carbon–carbon nanotube nanocomposite coatings for supercapacitor applications. *Surf. Coat. Technol.* **2013**, *232*, 326–330. [[CrossRef](#)]
7. Lekakou, C.; Moudam, O.; Markoulidis, F.; Andrews, T.; Watts, J.F.; Reed, G.T. Carbon-based fibrous EDLC capacitors and supercapacitors. *J. Nanotechnol.* **2011**, *2011*, 409382. [[CrossRef](#)]
8. Vermisoglou, E.C.; Giannakopoulou, T.; Romanos, G.; Giannouri, M.; Boukos, N.; Lei, C.; Lekakou, C.; Trapalis, C. Effect of hydrothermal reaction time and alkaline conditions on the electrochemical properties of reduced graphene oxide. *Appl. Surf. Sci.* **2015**, *358*, 100–109. [[CrossRef](#)]
9. Vermisoglou, E.C.; Giannakopoulou, T.; Romanos, G.F.; Boukos, N.; Giannouri, M.; Lei, C.; Lekakou, C.; Trapalis, C. Non-activated high surface area expanded graphite oxide for supercapacitors. *Appl. Surf. Sci.* **2015**, *358*, 110–121. [[CrossRef](#)]
10. Vermisoglou, E.C.; Giannakopoulou, T.; Romanos, G.; Boukos, N.; Psycharis, V.; Lei, C.; Lekakou, C.; Petridis, D.; Trapalis, C. Graphene-based materials via benzidine-assisted exfoliation and reduction of graphite oxide and their electrochemical properties. *Appl. Surf. Sci.* **2017**, *392*, 244–255. [[CrossRef](#)]
11. Reniers, J.M.; Mulder, G.; Howey, D.A. Review and performance comparison of mechanical-chemical degradation models for lithium-ion batteries. *J. Electrochem. Soc.* **2019**, *166*, A3189–A3200. [[CrossRef](#)]
12. Ozdogru, B.; Dykes, H.; Padwal, S.; Harimkar, S.; Çapraz, O. Electrochemical strain evolution in iron phosphate composite cathodes during lithium and sodium ion intercalation. *Electrochim. Acta* **2020**, *353*, 136594. [[CrossRef](#)]
13. Junga, D.H.; Kima, D.; Kimb, S.; Kima, T.W. Internal heat self-generation in lifepo4 battery module. *Appl. Sci. Converg. Technol.* **2020**, *29*, 94–97. [[CrossRef](#)]
14. Wang, C.-J.; Zhu, Y.-L.; Gao, F.; Qi, C.; Zhao, P.L.; Meng, Q.-F.; Wang, J.-Y.; Wu, Q.B. Thermal runaway behavior and features of LiFePO₄/graphite aged batteries under overcharge. *Int. J. Energy Res.* **2020**, *44*, 5477–5487. [[CrossRef](#)]
15. Du, Z.; Wood, D.L., III; Daniel, C.; Kalnaus, S.; Li, J. Understanding limiting factors in thick electrode performance as applied to high energy density Li-ion batteries. *J. Appl. Electrochem.* **2017**, *47*, 405–415. [[CrossRef](#)]
16. Frenck, L.; Sethi, G.K.; Maslyn, J.A.; Balsara, N.P. Factors that control the formation of dendrites and other morphologies on lithium metal anodes. *Front. Energy Res.* **2019**. [[CrossRef](#)]

17. Wang, T.; Li, Y.; Zhang, J.; Yan, K.; Jaumaux, P.; Yang, J.; Wang, C.; Shanmukaraj, D.; Sun, B.; Armand, M.; et al. Immunizing lithium metal anodes against dendrite growth using protein molecules to achieve high energy batteries. *Nat. Comm.* **2020**, *11*, 5429. [CrossRef]
18. Ruschhaupt, P.; Varzi, A.; Passerini, S. Greener supercapacitors: Aqueous binders and moisture tolerant electrolytes. *ECS Meet. Abstr.* **2020**, *3*, 609. [CrossRef]
19. Scalia, A.; Zaccagnini, P.; Armandi, M.; Latini, G.; Versaci, D.; Lanzio, V.; Varzi, A.; Passerini, A.; Lamberti, A. Tragacanth gum as green binder for sustainable water-processable electrochemical capacitor. *ChemSusChem* **2021**, *14*, 356–362. [CrossRef]
20. Fields, R.; Lei, C.; Markoulidis, F.; Lekakou, C. The composite supercapacitor. *Energy Technol.* **2016**, *4*, 517–525. [CrossRef]
21. Markoulidis, F.; Dawe, A.; Lekakou, C. Electrochemical double-layer capacitors with lithium-ion electrolyte and electrode coatings with PEDOT: PSS binder. *J. Appl. Electrochem.* **2021**, *51*, 373–385. [CrossRef]
22. Cuesta, N.; Ramos, A.; Cameán, I.; Antuña, C.; García, A.B. Hydrocolloids as binders for graphite anodes of lithium-ion batteries. *Electrochim. Acta* **2015**, *155*, 140–147. [CrossRef]
23. Aguiló-Aguayo, N.; Hubmann, D.; Khan, F.U.; Arzbacher, S.; Bechtold, T. Water-based slurries for high-energy LiFePO₄ batteries using embroidered current collectors. *Sci. Rep.* **2020**, *10*, 5565. [CrossRef]
24. Jeong, S.S.; Böckenfeld, N.; Balducci, A.; Winter, M.; Passerini, S. Natural cellulose as binder for lithium battery electrodes. *J. Power Sources* **2012**, *199*, 331–335. [CrossRef]
25. La Monaca, A.; De Giorgio, F.; Focarete, M.L.; Fabiani, D.; Zaccaria, M.; Arbizzani, C. Polyvinylidene difluoride–polyethyleneoxide blends for electrospun separators in Li-ion batteries. *J. Electrochem. Soc.* **2017**, *164*, A6431–A6439. [CrossRef]
26. Elsayed, Y.; Lekakou, C.; Labeed, F.; Tomlins, P. Fabrication and characterisation of biomimetic, electrospun gelatin fibre scaffolds for tunica media-equivalent, tissue engineered vascular grafts. *Mater. Sci. Eng. C* **2016**, *61*, 473–483. [CrossRef]
27. Salifu, A.A.; Lekakou, C.; Labeed, F.H. Electrospun oriented gelatin-hydroxyapatite fiber scaffolds for bone tissue engineering. *J. Biomed. Mater. Res. Part A* **2017**, *105*, 1911–1926. [CrossRef]
28. Markoulidis, F.; Bates, J.; Lekakou, C.; Slade, R.; Laudone, G.M. Supercapacitors with lithium-ion electrolyte: An experimental study and design of the activated carbon electrodes via modelling and simulations. *Carbon* **2021**, *164*, 422–434. [CrossRef]
29. Bates, J.; Markoulidis, F.; Lekakou, C.; Laudone, G.M. Design of porous carbons for supercapacitor applications for different organic solvent-electrolytes. *C* **2021**, *7*, 15. [CrossRef]
30. Baboo, J.P.; Babar, S.; Kale, D.; Lekakou, C.; Laudone, G.M. Designing a graphene coating-based supercapacitor with lithium ion electrolyte: An experimental and computational study via multiscale modeling. *Nanomaterials* **2021**, *11*, 2899. [CrossRef]
31. Robinson, J.B.; Xi, K.; Kumar, R.V.; Ferrari, A.C.; Au, H.; Titirici, M.-M.; Parra-Puerto, A.; Kucernak, A.; Fitch, S.D.S.; Garcia-Araez, N.; et al. 2021 roadmap on lithium sulfur batteries. *J. Phys. Energy* **2021**, *3*, 031501. [CrossRef]
32. Lasetta, K.; Baboo, J.P.; Lekakou, C. Modeling and simulations of the sulfur infiltration in activated carbon fabrics during composite cathode fabrication for lithium-sulfur batteries. *J. Compos. Sci.* **2021**, *5*, 65. [CrossRef]
33. Grabe, S.; Baboo, J.P.; Tennison, S.; Zhang, T.; Lekakou, C.; Andritsos, E.I.; Cai, Q.; Downes, S.; Hinder, S.; Watts, J.F. Sulfur infiltration and allotrope formation in porous cathode hosts for lithium-sulfur batteries. *AIChE J.* **2022**. [CrossRef]
34. Dent, M.; Jakubczyk, E.; Zhang, T.; Lekakou, C. Kinetics of sulphur dissolution in lithium-sulphur batteries. *J. Phys. Energy* **2022**, *4*, 024001. Available online: <https://iopscience.iop.org/article/10.1088/2515-7655/ac521d> (accessed on 1 March 2022). [CrossRef]
35. Doyle, M.; Fuller, T.F.; Newman, J. Modeling of galvanostatic charge and discharge of the lithium/polymer/insertion cell. *J. Electrochem. Soc.* **1993**, *140*, 1526–1533. [CrossRef]
36. Fuller, T.F.; Doyle, M.; Newman, J. Simulation and optimization of the dual lithium ion insertion cell. *J. Electrochem. Soc.* **1994**, *141*, 1. [CrossRef]
37. Doyle, M.; Newman, J.; Gozdz, A.S.; Schmutz, C.N.; Tarascon, J.-M. Comparison of modeling predictions with experimental data from plastic lithium ion cells. *J. Electrochem. Soc.* **1996**, *143*, 1890–1903. [CrossRef]
38. Korotkin, I.; Sahu, S.; O’Kane, S.E.J.; Richardson, G.; Foster, J.M. Dandelion v1: An extremely fast solver for the Newman model of lithium-ion battery (dis)charge. *J. Electrochem. Soc.* **2021**, *168*, 060544. [CrossRef]
39. Gao, L.; Liu, S.; Dougal, R.A. Dynamic lithium-ion battery model for system simulation. *IEEE Trans. Compon. Packag. Technol.* **2002**, *25*, 495–505.
40. Chen, W.J.; Tan, X.J.; Cai, M. Parameter identification of equivalent circuit models for li ion batteries based on tree seeds algorithm. In Proceedings of the International Conference on Sustainable Energy Engineering, Perth, Australia, 12–14 June 2017; Volume 73, p. 012024. [CrossRef]
41. Tran, N.T.; Vilathgamuwa, M.; Farrell, T.; Choi, S.S. Matlab simulation of lithium ion cell using electrochemical single particle model. In Proceedings of the 2016 IEEE 2nd Annual Southern Power Electronics Conference (SPEC), Auckland, New Zealand, 5–8 December 2016; IEEE: Manhattan, NY, USA, 2017. [CrossRef]
42. Schimpe, M.; von Kuepach, M.E.; Naumann, M.; Hesse, H.C.; Smith, K.; Jossen, A. Comprehensive modeling of temperature-dependent degradation mechanisms in lithium iron phosphate batteries. *J. Electrochem. Soc.* **2018**, *165*, A181–A193. [CrossRef]
43. Safari, M.; Delacourt, C. Modeling of a commercial graphite/LiFePO₄ cell. *J. Electrochem. Soc.* **2011**, *158*, A562–A572. [CrossRef]
44. Rajabloo, B.; Jokar, A.; Desilets, M.; Lacroix, M. An inverse method for estimating the electrochemical parameters of lithium-ion batteries. *J. Electrochem. Soc.* **2017**, *164*, A99–A105. [CrossRef]
45. Lekakou, C.N.; Richardson, S.M. Simulation of reacting flow during filling in reaction injection molding (RIM). *Polym. Eng. Sci.* **1986**, *26*, 1264–1275. [CrossRef]

46. Elsayed, Y.; Lekakou, C.; Tomlins, P. Modeling, simulations, and optimization of smooth muscle cell tissue engineering for the production of vascular grafts. *Biotechnol. Bioeng.* **2019**, *116*, 1509–1522. [[CrossRef](#)]
47. Markoulidis, F.; Lei, C.; Lekakou, C. Investigations of activated carbon fabric-based supercapacitors with different interlayers via experiments and modelling of electrochemical processes of different timescales. *Electrochim. Acta* **2017**, *249*, 122–134. [[CrossRef](#)]
48. Muruges, A.K.; Uthayanan, A.; Lekakou, C. Electrophoresis and orientation of multiple wall carbon nanotubes in polymer solution. *Appl. Phys. A* **2010**, *100*, 135–144. [[CrossRef](#)]
49. Meng, M.; Yan, H.; Jiao, Y.; Wu, A.; Zhang, X.; Wang, R.; Tian, C. A “1-methylimidazole-fixation” route to anchor small-sized nitrides on carbon supports as non-Pt catalysts for the hydrogen evolution reaction. *RSC Adv.* **2016**, *6*, 29303–29307. [[CrossRef](#)]
50. Parimalam, B.S.; Lucht, B.L. Reduction reactions of electrolyte salts for lithium ion batteries: LiPF₆, LiBF₄, LiDFOB, LiBOB, and LiTFSI. *J. Electrochem. Soc.* **2018**, *165*, A251–A255. [[CrossRef](#)]
51. Lee, H.; Lim, H.-S.; Ren, X.; Yu, L.; Engelhard, M.H.; Han, K.S.; Lee, J.; Kim, H.-T.; Xiao, J.; Liu, J.; et al. Detrimental effects of chemical crossover from the lithium anode to cathode in rechargeable lithium metal batteries. *ACS Energy Lett.* **2018**, *3*, 2921–2930. [[CrossRef](#)]
52. Lyu, H.; Li, Y.; Jafta, C.J.; Bridges, C.A.; Meyer, H.M., III; Borisevich, A.; Paranthaman, M.P.; Dai, S.; Sun, X.-G. Bis(trimethylsilyl) 2-fluoromalonate derivatives as electrolyte additives for high voltage lithium ion batteries. *J. Power Sources* **2019**, *412*, 527–535. [[CrossRef](#)]
53. Galaguz, V.A.; Potapenko, O.V.; Panov, E.V. Diffusion characteristics of the LiFePO₄/C composite in an electrolyte based on LiBOB. *RREC* **2015**, *6*, 49–57.
54. An, S.J.; Li, J.; Daniel, C.; Mohanty, D.; Nagpure, S.; Wood, D.L., III. The state of understanding of the lithium-ion-battery graphite solid electrolyte interphase (SEI) and its relationship to formation cycling. *Carbon* **2016**, *105*, 52–76. [[CrossRef](#)]
55. Mercer, M.P.; Otero, M.; Ferrer-Huerta, M.; Sigal, A.; Barraco, D.E.; Hoster, H.E.; Leiva, E.P.M. Transitions of lithium occupation in graphite: A physically informed model in the dilute lithium occupation limit supported by electrochemical and thermodynamic measurements. *Electrochim. Acta* **2019**, *324*, 134774. [[CrossRef](#)]
56. Antonopoulos, B.K.; Stock, C.; Maglia, F.; Hoster, H.E. Solid electrolyte interphase: Can faster formation at lower potentials yield better performance? *Electrochim. Acta* **2018**, *269*, 331–339. [[CrossRef](#)]
57. Gavilán-Arriazu, E.M.; Mercer, M.P.; Pinto, O.A.; Oviedo, O.A.; Barraco, D.E.; Hoster, H.E.; Leiva, E.P.M. Effect of temperature on the kinetics of electrochemical insertion of Li-ions into a graphite electrode studied by kinetic Monte Carlo. *J. Electrochem. Soc.* **2020**, *167*, 013533. [[CrossRef](#)]